DNS OF MICROJETS FOR TURBULENT BOUNDARY LAYER CONTROL

Conrad Y. Lee [1] and David B. Goldstein [2]

Center for Aeromechanics Research

Department of Aerospace Engineering & Engineering Mechanics

The University of Texas at Austin

Austin, TX 78712-1085

Turbulent boundary layer flow may be controlled using microjets to alter the fine scale flow structures. In the present work, a direct numerical simulation of a turbulent boundary layer is coupled with an immersed boundary method to simulate the detailed shape and actuator motion of an array of synthetic jet MEMS. Results show that the inactive low profile MEMS devices have a weak effect on the boundary layer. Time-averaged data from quasi-steady and continuously pulsed actuation show how the jet arrays affect the boundary layer in the long run while instantaneous data show the formation of the three-dimensional jets in detail and their interaction with local structures.

1 Introduction

A turbulent boundary layer may seem to be characterized by random fluctuations of velocity and pressure but in reality those fluctuations are associated with vortical structures that arise, evolve and decay in a quasi-periodic fashion. As highlighted in Panton [1], within the region $y^+ < 100$, these vortices form a self-sustaining mechanism that continuously breaks down and creates more vortical structures through interactions with the surface. Of particular interest are the streamwise vortices that often originate from the formation and stretching of symmetric and asymmetric horseshoe vortices. Streamwise vortices are usually accepted as having core diameters of 10 to 40 wall units, lengths of O(100) wall units and cores 10 to 50 wall units above the wall. Counter-rotating vortex pairs, roughly 50 wall units apart, lead to the formation of low speed streaks about 10 to 40 wall units wide and O(1000) wall units long. Such low speed streaks are believed to be responsible for the breakdown and eruption of the wall layer – a key mechanism in the production of new vortical structures and the increase in shear stress at the wall. However, despite the existence of this and other models describing turbulence production, proof of the entire cyclic process, through conclusive experimental and computational observations, has not yet been obtained. This lack of conclusive observations is all the more clear if the surface is not flat but has passive textures or active control devices. For any attempt at boundary layer control to be successful, both a greater understanding of turbulent boundary layer structures and their interaction with passive and active elements is needed. The present paper represents an initial attempt at examining the interaction of a particular control device with the turbulent near-wall structures.

Advances in micro-machining and etching techniques have allowed the construction and testing of several MEMS (Micro Electronic Mechanical Systems) devices for flow control as reviewed by Gad-el-Hak [2] and described in detail in several other studies. For example, Cattafesta *et al.* [3] has constructed and tested microflaps which are being considered for use in flow control of micro air vehicles. Relatively large synthetic jets have been used by Smith *et al.* [4] to maintain attached flow past the stall angle-of-attack of an airfoil and reduce pressure drag by as much as 40%. Similar results with synthetic jets on flow over cylinders were obtained by Crook *et al.* [5]. Among the different types of MEMS for flow control, synthetic jets are of particular interest for distributed turbulent boundary layer control because they are zero-net-mass flux, low profile and sturdy devices requiring no internal fluid supply lines. The design and performance of both isolated and paired synthetic jets were analyzed experimentally by Smith and Glezer [6] and Smith *et al.* [7] and complemented by numerical simulations of near-isolated 2-D and 3-D jets such as Rizzetta *et al.* [8], 2-D studies of single (Kral *et al.* [9]), and paired jets (Guo *et al.* [10]) and 2-D arrays of jets (Lee and Goldstein [11]). Arrays of such devices coupled with sensors and prediction algorithms have been constructed and tested by Breuer *et al.* [12] and Tardu [13] with reported local reductions in shear stress on a flat plate.

For numerical studies of turbulent boundary layers, schemes that allow direct numerical simulation (DNS) of the Navier-Stokes equations have been used

[1] Graduate Research Assistant, Student Member AIAA

[2] Associate Professor, Senior Member AIAA

to complement and expand data acquired through experiments. DNS has allowed the development of data reduction techniques that better detect and identify the vortical structures in a turbulent boundary layer (Jeong *et al.* [14]). A next step is to combine turbulent flow DNS with arrays of actuators/sensors. Choi *et al.* [15] has combined DNS of turbulent channel flow with an opposition control scheme based on creating a dampening virtual wall above the actual surface. The virtual wall limits the wall-normal velocity fluctuations of the flow with an overall result said to be similar to suction and blowing near the solid surface, even though no detailed actuator motion is modeled. With a great deal of knowledge of the flow, an optimum control surface can be calculated and applied at each time step to limit the formation of and eliminate near wall coherent structures. This method has been shown by Koumoutsakos *et al.* [16] to reduce flat plate drag by 20% to 25% depending on where the control was applied and has been successfully used with large eddy simulations by Chang and Collis [17].

So far, the potential of synthetic jets for turbulent boundary layer drag reduction has been suggested both experimentally and numerically. However, a full simulation involving DNS of turbulent flow, the detailed physics of the jets and their interaction with the bulk flow has yet to be attempted. Simulating the inner cavity, actuating membranes and orifice geometry may be important since previous numerical studies show that the resulting flow is highly dependent on both the fluid parameters and geometric parameters of the device (Lee and Goldstein [11]). Thus, an alternate DNS method capable of achieving such detailed modeling is presented so that the jet formation process and its impact on a turbulent boundary layer can be better understood. This study may allow the design of more efficient actuators as well as give insight into the optimum density, operation and placement of actuator/sensor clusters. Preliminary results for several simple cases are presented.

At the scale of the devices themselves, the jets are expected to operate at a very low local Reynolds number even though the boundary layer Re may be large. The Re_{jet} defined according to microjet parameters is:

$$Re_{jet} = \frac{u_{peak} h_{1/2}}{\nu} \approx O(10) \tag{1}$$

where $h_{1/2}$ is the jet half-width, ν is the kinematic viscosity and u_{peak} is the average jet velocity at peak blowing across the slit. Similar parameters are used to define the Strouhal number:

$$St_{jet} = \frac{2\pi f h_{1/2}}{u_{peak}} \tag{2}$$

where f is the pulsing frequency of the actuator.

The computational approach is summarized in Sec. 2.1 with the construction of the actuators described in Sec. 2.2. Convergence issues and results for no actuation, steady actuation and pulsing actuation follow (Sec 3.1 through 3.5).

2 Numerical Procedure

2.1 The DNS method

The DNS method used in this simulation is based on that developed by Kim *et al.* [18] and adopted by Handler *et al.* [19] to examine turbulent channel flow. The incompressible Navier-Stokes equations are manipulated into a system of equations involving velocity and vorticity. The equations are solved with a Chebyshev-tau method with cosine grid clustering in the wall-normal direction. Time stepping is done with an Adams-Bashforth scheme for the non-linear terms and Crank-Nicholson for the viscous terms. Spectral representations make this method attractive for DNS of turbulence due to the low computational cost of fast transform methods and for the accuracy of results in smooth flows.

Modifications made to the code allow the use of virtual surfaces to define both the solid and moving walls. This method, related to that of Peskin [20] and developed by Goldstein *et al.* [21,22], imposes a localized body force along desired points in the computational mesh to bring the fluid there to a specified velocity so that the force has the same effect as a solid boundary. The desired velocity is incorporated in an iterative feedback loop to determine the appropriate force. For example, given a moving boundary with velocity $U_{desired}(x_s, t)$, a suitable expression for the body force is:

$$F_s(x_s, t) = \alpha \int_0^t (\Delta U_s) dt' + \beta(\Delta U_s) \tag{3}$$

where F_s corresponds to the value of the body force at specified boundary points x_s. ΔU_s is the difference between the fluid velocity and the desired velocity at the boundary points:

$$\Delta U_s = U_s(x_s, t) - U_{desired}(x_s, t) \tag{4}$$

and if the boundary is stationary, $U_{desired}$ is zero.

The constants α and β are negative and defined as the gain and damping of the force field with dimensions of $M/(L^3T^2)$ and $M/(L^3T)$, respectively. Throughout the study, the gain and damping of the force field are left at 20.

This virtual surface approach allows for fairly complex geometries and moving boundaries to be incorporated in a regular domain without the usual complexities of mapping. Previous studies by Goldstein and Tuan [23] confirmed the success of this technique for modeling a riblet surface below a turbulent boundary layer with only a 5% increase in computational time when compared to conventional boundary definitions of a solid flat surface. Moreover, that study also demonstrated that grid-converged solutions for turbulent flow could be obtained even with virtual surfaces in the flow.

2.2 Actuator Modeling

The problem of interest is that of a cluster of actuators centered on one wall of a channel that is periodic in both the streamwise and cross flow directions. A schematic of the computational domain is shown in fig. 1(a) while the details of the sub-surface actuator array are shown in Fig. 1(b). Each actuator consists of two slot jets powered by a common membrane so that the adjacent jets are coupled 180^o degrees out of phase. The initial channel geometry has a grid of $128 \times 65 \times 128$ cells in the x, y, z directions respectively. The domain is periodic in the (Fourier) x and z directions with the channel boundaries as horizontal y-planes (in the in-homogeneous Chebyshev direction). A bulk flow may be driven in the x-direction with a constant gravitational force. A virtual plate containing four slots having an aspect ratio of 16, with a width $h = 6$ gridcells[3] in z and a length $L = 20$ gridcells[3] in x, is placed 9 gridcells[4] above the bottom of the channel with the force field method. The virtual plate is two gridcells thick which corresponds to a thickness of $1.2h$ – a needed design condition since previous studies (Lee and Goldstein [11]) showed that microjet performance is influenced by the thickness and shape of the lips and most devices used in experiments have flat, thick lips.

In the space between the plate and the channel wall, dividing walls spanning the length of the domain are placed to create the four jet cavities corresponding to two pairs of actuators. These walls are defined as shear-free walls that allow fluid motion in the x and y-direction but no penetration in the z-direction. These shear-free conditions are necessary to reduce Gibbs phenomena that creates "ghost" impressions of the internal geometry above the plate. A rectangular section of the shear-free wall spanning the height of the cavity and measuring two slot lengths long is designated as the moving membrane (fig. 1(b)). To simulate the membrane motion, the magnitude of the z-velocity specified with the force field on this section is shaped with a sine^2 distribution. Since the fluid is incompressible and the domain periodic in the x-direction, the spanwise sub-surface mass fluxes in the z-direction through the membrane create net mass fluxes through the slots.

[3] on the 3/2's de-aliased grid

[4] no de-aliasing in the y-direction

3 Results

3.1 Convergence Issues

An initial fully developed turbulent channel flow was used as the starting point of the simulations. Throughout this study, $Re_{channel}$, the Reynolds number defined according to the channel half-height and centerline velocity is about $2,200$ while R^*, the Re defined according to the friction velocity u^* and channel half-height is about 119. For comparison purposes, the friction velocity u^*, viscous length scale l^* and viscous time scale $t^* = l^*/u^*$ obtained from the above flow parameters are taken as constants and used throughout this study whenever friction properties are needed to normalize data or figures. The channel dimensions, in wall units, are then $1,500l^* \times 238l^* \times 290l^*$ in the x, y, z directions, respectively. The grid spacings in the streamwise and spanwise directions are, respectively, $\Delta x^* = 11.7$ and $\Delta z^* = 2.3$, comparable to the studies by Kim *et al.* [18] where $\Delta x^* = 12$ and $\Delta z^* = 7.0$. We use a finer scale in the spanwise z-direction to better resolve the flow near the slots. The slot width is $9.1l^*$, similar to the size of the devices used in experiments by Breuer *et al.* [12]. Goldstein *et al.* [21] and Goldstein and Tuan [23] showed that the combination of turbulent channel DNS and virtual force method, on the same or coarser grids is converged for flow over riblets and wires at the above values of $Re_{channel}$ and R^*. Moreover, Goldstein, *et al.* [22] simulated turbulent flow over a virtual flat plate placed at 15 gridcells above the bottom of the channel, (compared to the current 9 gridcells) and found excellent agreement with simulations done without virtual surfaces. Consequently, the near-wall vertical cell spacing we use (Δy) should be adequate in the present simulations.

Thus, by comparison to these earlier studies using the same numerical method, the present spatial resolution should be adequate to model a turbulent boundary layer. The virtual force method applied to 2-D slot jets has also been shown, in our earlier study (Lee and Goldstein [11]), to converge for Re_{jet} less than or equal to 416. We thus assume that the present results converge as well since Re_{jet} is never larger than 34. Moreover, at the highest Re_{jet}, the cell Reynolds number based on the cell dimension in the direction of highest gradient in the region of the slot is three

times smaller in the present simulations than in Lee and Goldstein [11]. We have also found in [11] that low Re_{jet} 2-D synthetic jets were time-resolved with time steps smaller than $1/1000^{th}$ of the period of actuation and the same criteria is maintained for this study as well. The actual time step Δt corresponds to $0.03t^*$ – a conservative value for turbulent boundary layer simulations.

3.2 Effect of the Inactive Devices

The new geometry with the virtual plate and internal structure is inserted abruptly in the fully developed flow and the simulation allowed to run for $20,000$ time steps to stabilize once more. For this first part of the study, no actuation is applied by the membrane to create jets. Results after stabilization are shown in figure 2 as contours of normalized streamwise velocity on an xy-plane through the slots and in figure 3 as contours of normalized v velocity in an xz-plane $4l^*$ above the virtual plate. Both figures show the development of a new boundary layer over the virtual plate with the usual features and characteristics of turbulent flow. Figure 2 indicates that the fluid under the virtual plate is essentially stationary (dark blue). There is also negligible interaction between the cavity fluid and the external region at this location. Figure 3 shows a few flow structures present at the center of the channel that hint at the presence of the slots. It is believed that these velocity traces are a result of interaction of buffer layer vortices with the sharp edges of the slots creating weak transient separated regions. Flow visualization of instantaneous vorticity in the streamwise direction (Ω_x) is shown in figure 4. The figure depicts a section of the channel spanning the x and z directions but cropped at $y^+ = 70$ in the normal direction with the virtual plate placed at $y^+ = 0$. There is no indication of the presence of the slots and the few worm-like structures are spread out somewhat uniformly over the channel. For comparison purposes, fig. 4 and all other subsequent plots involving vorticity are normalized with the same h/u_{cl} parameter set constant at 0.43.

Flow properties are averaged over the next $60,000$ time steps ($1,760t^*$) and the results further shows no mean effects of the presence of the slots. Figure 5 contains a time-averaged iso-surface corresponding to a streamwise velocity of $u^+ = 4$. The iso-surface is nearly smooth with negligible visible disturbances. This demonstrates that when unactuated, such low profile devices, despite some occasional instantaneous local disturbances (fig. 3), do not to have an overall effect on a turbulent boundary layer. Drag over the virtual surface is obtained by calculating an instantaneous momentum balance over the entire length of the channel and subtracting the known drag over the top boundary. The drag ratio between the top boundary and the virtual surface can then be used to gauge the effectiveness of the devices for reducing drag. In this case with no actuation, the drag for the virtual wall was $5 \pm 6\%$ lower than the top wall – a negligible difference. This case must yet be run further in time, still it is clear that the inactive small slots have negligible influence on the turbulent flow.

3.3 Pulsed Jet Operation in the Absence of Channel Flow

The devices are next tested without the bulk channel flow to give insight into the characteristics of the 3-D jets. The simulation is begun with a quiescent flow and no mean gravity force acting down the channel. A smooth periodic sinusoid is applied to the normal velocity of the membrane. Given the construction of the devices which couples each pair of jets 180^o out-of-phase, various modes of actuation are possible. We examine first the "-++-" mode, in which the jets are initially operated with in-phase blowing out of the two center slots and suction through the two outer slots. As the device continues to operate, the pumping membranes reverse direction (as per the temporally sinusoidal membrane force field) and the opposite actuation occurs with suction through the two center slots and blowing out of the outer slots. The second mode, "-+-+," involves pulsing the devices with alternating blowing and suctioning slots. In both modes, the magnitude of the pumping membrane is set to create a jet of area-averaged velocity at peak blowing of $7.5u^*$ and the period of actuation $T = 30t^*$ for a Strouhal number of 0.13. Recall that the friction properties are those which occur with the turbulent boundary layer simulation in Sec. 3.1. The corresponding Re_{jet} for this case is 34, considerably larger than needed for boundary layer control in which we expect that blowing speeds closer to the turbulent boundary layer turbulent fluctuations (1 to $3u^*$) are needed. A blowing speed of $7.5u^*$ is, however, useful to visualize jet interaction effects.

Results for the "-++-" mode are shown in figures 6 and 7. Figure 6 shows contours of normalized Ω_x vorticity on a zy-plane through the center of the slots after 4.5 pumping cycles (top figure) and then half a cycle later (bottom figure). The colors are saturated to enhance contrast and as a result Gibbs phenomena have been highlighted as well. Black lines represent stationary solid boundaries while white lines represent the moving virtual membrane. Figures 7(a) and (b) show corresponding iso-surface contours of the magni-

tude of normalized vorticity (enstrophy) in the channel below $y^+ = 70$ for the same times. The virtual plate containing the four slots is identified as the bottom plane ($y^+ = 0$). As found by Rizzetta *et al.* [8], the 3-D slot jet begins as a rectangular ring vortex composed of the vortex sheets created by fluid separating at the outer edges of the slot (fig. 6). However, unlike the isolated slot jet studies of Rizzetta *et al.* [8], the current simulation involves closely coupled arrays of microjets and the subsequent results reflect that proximity. For central blowing (top fig. 6), the jets have a tendency to move apart due to the proximity of the two sets of similar vortical structures and the outboard suction. This result is similar to but not as pronounced as what was observed in the previous 2-D simulation of arrays of paired jets (Lee and Goldstein [11]). Similar vorticity is generated at the slot lips as fluid is drawn into the cavity at the outer slots but it dissipates against the internal walls of the cavity and the pumping membrane. Vorticity produced in the first half pumping cycle ($t = 0$ to $T/2$) is found to remain coherent up to $150l^*$ above the plate. As the microjets continue to operate through later cycles ($t > T/2$), subsequent vortex cores tend to be confined to, or diffuse away, within $100l^*$ above the plate. This difference is believed to be a result of the starting condition of the simulation: while the first pulse discharges into quiescent fluid and is free to translate upward under self-induced motion, subsequent pulses encounter leftover vorticity from previous cycles that affect their trajectory and dissipation rate.

Rizzetta *et al.* [8] showed that their initial 3-D jet shape resembled a "bread loaf" but fig. 7(a) shows that the current 3-D jet shape has thick, bulbous ends. This enhanced outflow near the slot ends is believed to be a result of the shape of the cavity and elongated membrane: fluid in the cavity is pushed nearly uniformly along the membrane surface so that a mass of fluid near the center of the slot can readily exit the cavity. But, near the ends of the slot, more fluid must squeeze out since the membrane is twice as long as the slot. This fluid, moreover, encounters an area constriction near the slot ends yet it must exit the cavity since the fluid is incompressible. The net result is that fluid near the edge of the slot exits more forcefully and leads to the end distortion in the jet shape. The locations of suctioning slots are also visible in figure 7 as layers of enstrophy being drawn into the cavity. In the case of outside blowing ("$+--+$," bottom fig. 6), the resulting jets are drawn towards the center suctioning slots so that their trajectories are tilted towards the center of the channel as they translate upward. This result is not entirely surprising since two adjacent slender slots with opposite actuation produce a certain amount of flow in the spanwise direction going from the blowing to the suctioning slot. Similar to the "$-++-$" pulses, the later "$+--+$" vorticity remains confined to within $100l^*$ above the plate. The corresponding 3-D jet shape shown in fig. 7(b) is also similar to what is observed in fig. 7(a) but with the jets tilted towards the inside suctioning slots.

Results for the "$-+-+$" mode are shown in figures 8 and 9, again as contours of normalized Ω_x vorticity and iso-surfaces of enstrophy. The jets in fig. 8 are shown after 4.5 pumping cycles (top figure, "$-+-+$" actuation) and again a half cycle later (bottom, "$+-+-$" actuation). Similar to the ("$-++-$") mode, the jets (fig. 8) are drawn slightly towards the adjacent suctioning slot. Also similar to the previous case, the initial blowing jets into quiescent flow persist up to $150l^*$ above the plate while subsequent vorticity extends to only $100l^*$ above the plate. As seen in fig. 8, despite the initial differences in the behavior of jets, there is a near mirror symmetry in the vortical structures between the "$-+-+$" and "$+-+-$" actuations after a few pumping cycles. The corresponding jet shape for the "$-+-+$" actuation is shown in fig. 9. The jets show similar bulbous end distortions and similar jet shapes are observed for the "$+-+-$" actuation but are not shown.

3.4 Quasi-Steady Actuation

Simulations of the two previous modes of operation ("$-++-$" and "$-+-+$") are next repeated with the addition of the mean channel flow and a fully developed turbulent boundary layer over the virtual plate as described in Sec 3.2. The membranes are set to undergo motion having a half-square wave amplitude (*i.e.*, the membrane pushes right for $0.4\,T$, stops for $0.6\,T$, then resumes pushing right so that the jets go only in one direction). The jet has an area averaged normal velocity of $1.8u^*$ at the slot plane during membrane motion and a Re_{jet} of 8.2. This blowing is four times weaker than that used in the previous section but is like that of the devices used in the experiments of Breuer *et al.* [12]. The period of oscillation (T) is 176 times larger than the viscous time scale t^*, giving a St_{jet} of 0.11 and making the actuation quasi-steady at any given point in the cycle.

Consider first the case with "$-++-$" blowing. Figure 10 shows the instantaneous contours of streamwise velocity on a zy-plane cutting through the center of the slots at $T/10$. As in previous figures of this type, black lines represent solid walls and white lines represent the pumping membrane wall. It can be seen that fluid sucked into the cavity retains some of its streamwise

momentum below the surface while ejected fluid has negligible streamwise momentum. This suggests that actuator modeling which produces simply wall-normal boundary suction/blowing (such as Kral *et al.* [9] and Guo *et al.* [10]) may not be an adequate representation for understanding the interaction of a small jet with the near-wall boundary layer turbulence. Similar zy-plane results are observed in the other quasi-steady types of actuation ("$+--+$" and "$-+-+$") but are not shown. Fig. 10 also show that the jet remains confined to $y^+ \leq 10$, well within the viscous sublayer. In fact, contours of vorticity on the same zy-plane, although not shown, demonstrate that the vorticity generated by the outflow dissipates quickly without forming an actual jet. This result is also illustrated in the 3-D visualization of the channel flow discussed below.

Figure 11 shows instantaneous Ω_x iso-surfaces $T/10$ into the first cycle of actuation. Recall that visualization of the turbulent flow with the devices non-operational in Sec. 3.2 showed vortical structures spread somewhat uniformly over the channel. As seen in fig. 11, however, the blowing center jets are identifiable as a series of small bumps. There are also raised bumps showing the vorticity layer being sucked into the cavities at the two outer slots. While the jet iso-surfaces barely register in the figure at later times well after the blowing is started, there are here appreciable disturbances created by the abrupt start of the jets seen downstream of the slots as several interesting vortical structures concentrated around the center of the channel. As they convect down the channel, the vortical structures diffuse and interact with each other leading to occasional lifting vortices such as seen near the end of the domain. As the jets continue to operate and are eventually turned off, no further substantial vorticity production is observed and the disturbances initially generated diffuse to the point that very few of them remain at the start of the next cycle. Data averaging was performed over $30,000$ time steps (6 pumping cycles) and the result is shown in figure 12 as an iso-surface of streamwise velocity u^+ in a section of the channel. For the "$-++-$" case, the center blowing jets appear as "shark fins" deformed by convection and shearing of the mean flow. The streak pattern shows the presence of at least four narrow low speed streaks (indicated by arrows in fig. 12). One pair of streaks are narrow and are located just inside of the two outer (sucking) slots. The other pair is less pronounced and is formed just outside of the two outer slots.

The reverse actuation case, with suction down the center slots ("$+--+$") is shown in fig. 13 as instantaneous contours of Ω_x, $T/10$ into the first pumping cycle. Note that the flowfield here was identical to that in the fig. 11 case before the jets were activated. Similar to the "$-++-$" case, the outer blowing jets are seen as a series of raised bumps and the vortex layer is being drawn into the cavity at the two center slots. The abrupt start of the jets does not create as much disturbance in the channel as seen previously in fig. 10. Time averaged results, again over $30,000$ time steps, are shown as a $u^+ = 4$ iso-surface in fig. 14. The outer blowing jets are clearly seen as the same "shark fins," albeit slightly shorter than the ones seen in the previous case (fig.12) while the streak pattern shows the presence of a single pair of wide low speed streaks directly over the outer slots. The difference between the height of the "shark fin" disturbances probably results from the mutual re-enforcement of the blowing jets for the "$-++-$" case and the lack thereof for the more distant jets for "$+--+$" actuation. While the streak pattern may be a characteristic of the actuation mode, the overall presence of low-speed streaks is to be expected from a quasi-steady blowing jet.

3.5 Periodic Pulsed Actuation

Studies of the effect of pulsed jets on a turbulent boundary layer were performed with the same actuation modes as in Section 3.3 ("$-++-$" and "$-+-+$" modes). Unlike the step-like quasi-steady actuation used in Sec. 3.4, the smooth periodic actuation used to study the 3-D jets in Sec. 3.3 is also applied to this section. The full period of oscillation (T), in which a given slot goes through a full cycle of blowing and sucking, corresponds to approximately $30t^*$. The pulses are not expected to be independent of each other since the channel flow-through time at the centerline of the channel or even at the height of streamwise vortices ($y^+ \approx 15$) are only $85t^*$ and $154t^*$, respectively. The pumping membrane is set to generate a modestly strong jet of area-averaged peak normal velocity corresponding to $3u^*$ for a Re_{jet} of 13.6 and a St_{jet} of 0.33. These values are at the upper limit of jet strength expected to be useful for turbulent boundary layer control. To date, only the effects of continuous pulsing have been examined but further detailed studies on the effect of individual pulses are planned for the future.

Instantaneous results taken from animations[5] for the "$-++-$" mode are shown in figures 15 and 16 as iso-surfaces of normalized enstrophy in a channel section below $y^+ = 70$. Figure 15 corresponds to the end of the first cycle of activation ($t = T$). Turbulent boundary layer structures can be seen as small lumps of enstrophy near the front of the domain or as the large,

[5] several animations are available for viewing/download at *http://www.ae.utexas.edu/~conlee/cfd/cfd.html*

elongated pancake structures sliding over the virtual plate. Similar to the the results of Sec. 3.3, the center blowing slots generate blowing jets with thick, bulbous ends which roll up into hairpin vortices. The suctioning slots can be seen as rectangular gaps in enstrophy outlined with the vortex layer created by suction. Unlike the results of Sec. 3.3, however, the blowing jets do not exhibit a tendency to move well above the wall. Rather, the jets are turned downstream by shearing of the mean flow. This effect of shear is particularly evident on the leading edge hairpins, which appear flatter and more stretched than the more shielded trailing hairpins. As the jet rises, the top of the lead hairpin reaches into a higher momentum flow before the rest of the jet and it rolls up into a classic hairpin vortex over the low-(streamwise) speed jet fluid. This phenomena causes the leading portion of the jets to flatten, translate downstream and rise faster than the trailing portion. Animations of this process indicate that much of the low speed fluid in the jet is subjected to Kelvin-Helmholtz instability which might, in some cases, roll up into a family of hairpins. In the present case, the single leading edge hairpin dominates, sometimes overtaking and swallowing weaker hairpins or as in the case shown in fig. 16, leap-frogging over the trailing edge hairpin. As the simulation is allowed to continue, the center blowing jets remain obviously coherent up to $50l^*$ above the virtual plate before breaking down into other structures within $200l^*$ downstream of the location of the slots. While the jets themselves may dissipate, their effects remain in the altered evolution of the pancake boundary layer structures.

As the jets continue to operate, the opposite actuation ("$+--+$") ensues. A typical result is shown in the iso-surfaces of enstrophy of fig. 16, taken at the end of the fourth full pumping cycle ($t = 4\,T$). The far (left) blowing jet shows a similar shape as the center jets of fig. 15, with a flattened hairpin at the leading edge. The hairpin evolution and decay also follow what was previously described. However, the close (right) blowing jet actuates directly on the trailing edge of a pancake boundary layer structure, causing it to rise like a tent over the rough shape of the jet. This jet/pancake vortex interaction is observed, shortly thereafter, to generate several tendril-structures of enstrophy that rise and dissipate and a thicker flat structure near the plate that remains in the channel for as long as $1000l^*$ past the location of the slots. Similar structures and rising tendrils are observed to result from the interaction of other pulses and boundary layer structures but are not shown.

Time averaged data over $80,000$ time steps (80 full pumping cycles) are shown in figure 17 as an iso-surface corresponding to $u^+ = 4$. The periodic jets do not quite average out due to data being sampled at a constant time interval at the end of a pumping cycle. Consequently the slot locations are still discernible as the slight bump and divot in the figure. Figure 17 shows no low speed streaks along the channel: the iso-surface is relatively smooth with only minor disturbances distributed over the channel. The calculated average drag over the same long time interval is $12 \pm 5\%$ higher than for the opposing flat wall. This large drag increase is not surprising in that the continuously pulsed periodic jets clearly cause strong vertical mixing of the streamwise momentum. It is somewhat surprising, however, there we find no obvious regions of either reduced or increased mean surface shear in the wake of the actuators while Breuer *et al.* [12] measured a 7% reduction in shear stress at a control location downstream of the actuators. This result is still being investigated at this time.

Results for the "$-+-+$" case are shown in figures 18 and 19 as instantaneous iso-surfaces of enstrophy. Figure 18 shows the flow at $t = T$ (typical of "$-+-+$" actuation) while fig. 19 corresponds to $t = 3\,T$ (typical for "$+-+-$" actuation). In fig. 18, the far (left) jet discharge is nearly identical to was is seen in fig. 15 with the same flattened leading edge shape distorted by the mean flow. The jet structure quickly dissipates within $200l^*$ downstream of the slot location and remains below $y^+ = 50$. The near (right) jet discharges at the trailing portion of a flat boundary layer structure and its evolution, shown further in fig. 19, is markedly different than previous jets. The jet remains coherent past a height of $70l^*$, out of the field of view, and the leading edge accelerates past the trailing edge causing the jet to wrap over itself. As the leading edge hairpin exits through the top plane of the figure, it also leaves behind stretched leg tendrils extending down to the plate that persist as far as $400l^*$ downstream of the slots (fig. 19). Visualization over the following 5 pumping cycles did not indicate a repeat of this behavior but other boundary layer/jet interactions followed the pattern previously observed in the "$+-+-$" case. Time averaged data over $80,000$ time steps (80 periods) yields the iso-surface of streamwise velocity ($u^+ = 4$) seen in figure 20. Like the previous mode of actuation (fig. 17), these "$-+-+$" pulsing jets show no mean streaks or major structures in the flow. The drag increase calculated for this "$-+-+$" mode is $15 \pm 7\%$, the same as the "$-++-$ mode. This suggests that the drag increase maybe independent of the pulsing mode and is a result of the particular type of actuation of the devices.

4 Discussion

An immersed boundary method was successfully integrated into a previously validated turbulent boundary layer DNS code to simulate the presence of an array of micro-jet actuators. There was a wide range of actuators and modes of operation one could explore. We chose to examine a four slot array of jets in which each adjacent pair of slots functioned as a single unit powered by a common membrane. The slot dimensions and mode of operation should be physically realizable. The slots should also interact with the turbulent boundary layer coherent structures at roughly the correct time and length scales suitable for flow control and, potentially, future drag reductions studies. No closed-loop control was attempted. For now, we simply wished to model fairly typical actuators and study their effects.

Our results confirm that such low profile, recessed actuators do not appreciably disturb the flow when they are inactive. We next examined sinusoidally actuated jets pulsed into a quiescent external domain. Cross flow views showed that adjacent synthetic jets repel each other by mutual interference while separated jet cores tend to be attracted by the nearby suctioning slot. This result is, of course, dependent on the exact slot geometry. However, the overall trend of vortex dynamics appears consistent with what others have observed in related studies (Smith *et al.* [7], Guo *et al.* [10] and Lee and Goldstein [11]). Three-dimensional views of enstrophy surfaces suggest similar results to those of Rizzetta *et al.* [8] except that in our case, the sub-surface flow causes higher velocity ejection towards the ends of the slot and this induces instability in the ejected plume. Should a more uniform exit velocity profile be desired, the driving membrane or the slot shape can be altered accordingly.

In contrast, weak jets ($1.8u^*$) of one orientation in quasi-steady operation discharging into a turbulent channel flow show no obvious near-field interaction with each other. Such actuation produces a mean streak pattern near the wall. Although the abrupt starting process for these jets produced a wide range of odd structures, during steady blowing, the jets were confined to the linear sublayer and consequently are unlikely to effectively manipulate directly other turbulent boundary layer structures. A moderately stronger jet ($3u^*$) in continuously pulsed operation was able to penetrate the boundary layer up to the buffer region and cause substantial change in the events of the boundary layer. Both "-++-" and "-+-+" sinusoidal actuation increased vorticity ejection and led to a substantial increase in drag. As each jet was turned on, the mean flow shear stress was found to cause a hairpin vortex to form near both the leading and trailing edges of the slug of ejected fluid. The legs of the hairpin and other vortex structures created by the jets seem to be narrower than the natural streamwise vortices in the turbulent boundary layer and, hence, they dissipated more readily.

The current study has given valuable insight on the performance of the 3-D array of actuators. Further studies targeting control of specific boundary layer structures are underway.

Acknowledgements

This work was supported by the Air Force Office of Scientific Research, grant F49620-98-1-0027.

References

[1] Panton, R., *Self-Sustaining Mechanisms of Wall Turbulence*, Computational Mechanics Publications, 1997, Chapters 2 and 3.

[2] Gad-el-Hak, M., "Modern Developments in Flow Control," *Appl. Mech. Rev.*, Vol. 49, No. 7, pp. 365-379, 1996.

[3] Cattafesta, L. N., III, Garg, S. and Washburn, A. E. "Piezoelectric Actuators for Fluid-Flow Control," Proceedings of the SPIE, Vol. 3044, pp. 147-157, 1997.

[4] Smith, D., Amitay, M., Kibens, V., Parekh, D. and Glezer, A., "Modification of Lifting Body Aerodynamics Using Synthetic Jet Actuators," 36th Aerospace Sci. Meeting, paper AIAA 98-0209, 1998.

[5] Crook, A., Sadri, A. M. and Wood, N. J., "The Development and Implementation of Synthetic Jets for the Control of Separated Flow," 17th Applied Aerodynamics Conf., paper AIAA 99-3176, 1999.

[6] Smith, B. L. and Glezer, A., "The Formation and Evolution of Synthetic Jets," *Physics of Fluids*, Vol. 10, No. 9, pp. 2281-2297, 1998.

[7] Smith, B. L., Trautman, M. A. and Glezer, A., "Controlled Interactions of Adjacent Synthetic Jets," 37th Aerospace Sci. Meeting, paper AIAA 99-0669, 1999.

[8] Rizzetta, D.P., Visbal, M.R. and Stanek, M.J., "Numerical Investigation of Synthetic Jet Flowfields," 29th AIAA Fluid Dyn. Conf., paper AIAA98-2910, 1998.

[9] Kral, L. D., Donovan, J. F., Cain, A. B. and Cary, A. W., "Numerical Simulation of Synthetic Jet Actuators," 28th AIAA Fluid Dyn. Conf. / 4th AIAA Shear Flow Control Conf., paper 97-1824, 1997.

[10] Guo, D., Kral, L. D., and Cary, A. W., "Numerical Simulation of the Interaction of Adjacent Synthetic Jet Actuators," 38th Aerospace Sci. Meeting, paper 2000-2565, 2000.

[11] Lee, C. and Goldstein, D. B., "Two-Dimensional Synthetic Jet Simulation," 38th Aerospace Sciences Meet., paper AIAA 2000-0406, 2000.

[12] Breuer, K. S., Amonlirdviman, K. and Rathnasingham, R., "Adaptive Feed-Forward Control of Turbulent Boundary Layers," 28th AIAA Aerospace Sciences Meeting, paper AIAA 98-1025, 1998.

[13] Tardu, S., "Local Oscillating Blowing in a Turbulent Boundary Layer," International Symposium on Seawater Drag Reduction, New Port, USA, 1998.

[14] Jeong, J., Hussain, F. and Kim, J., "Coherent Structures Near the Wall in a Turbulent Channel Flow," *J. Fluid Mech.*, Vol. 332, pp. 185-214, 1997.

[15] Choi, H., Moin, P. and Kim, J., "Active Turbulence Control for Drag Reduction in Wall-Bounded Flows," *J. Fluid Mech.*, vol. 262, p75-110, 1994.

[16] Koumoutsakos, P., Bewley, T. , Hammond, E. P. and Moin, P., "Feedback Algorithms for Turbulence Control – Some Recent Developments," paper AIAA 97-2008, 1997.

[17] Chang, Y. and Collis, S. S., "Active Control of Turbulent Channel Flows Based on Large Eddy Simulation," 3rd ASME/JSME Joint Fluids Eng. Conf. paper FEDSM99-6929, 1999.

[18] Kim, J., Moin, P. and Moser, R., "Turbulent statistics in fully developed channel flow at low Reynolds number," *J. Fluid Mech.*, vol. 177, p133-166, 1987.

[19] Handler, R. A., Hendricks, E. W. and Sirovich, L., "Low Reynolds Number Calculation of Turbulent Channel Flow: a General Discussion," NRL Mem. Rep. 6410, pp. 1-103, 1989.

[20] Peskin, C. S., "Flow Patterns Around Heart Valves: A Numerical Method," *J. of Comp. Physics*, Vol 10, p252-271, 1972.

[21] Goldstein, D., Handler, H. and Sirovich, L., "Direct numerical simulation of turbulent flow over a modeled riblet covered surface," *J. Fluid Mech.*, vol. 302, p333-376, 1995.

[22] Goldstein, D., Handler, H. and Sirovich, L., "Modeling a No-Slip Boundary with an External force Field," *J. of Comp. Physics*, vol. 105, p354, 1995.

[23] Goldstein, D., Tuan T.-C., "Secondary flow induced by riblets," *J. Fluid Mech.*, vol. 363, p115-151, 1998.

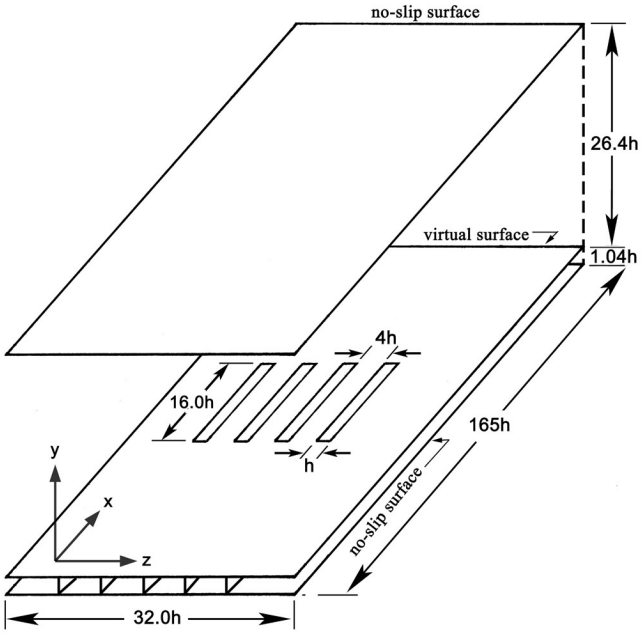

Figure 1(a): Schematic of channel and actuators

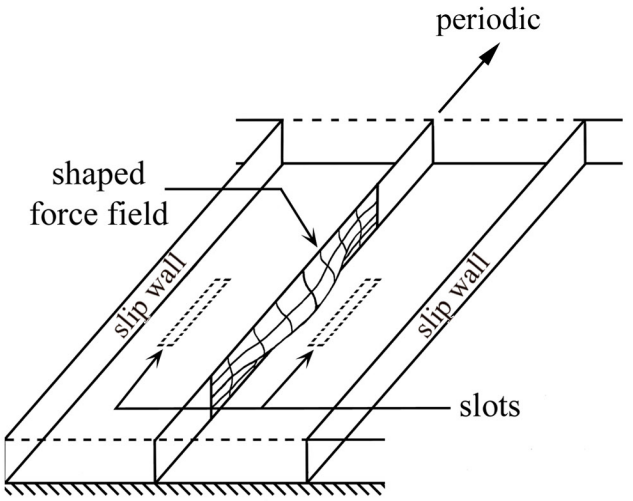

Figure 1(b): Schematic of single actuator array and sample force field shape for membrane deformation

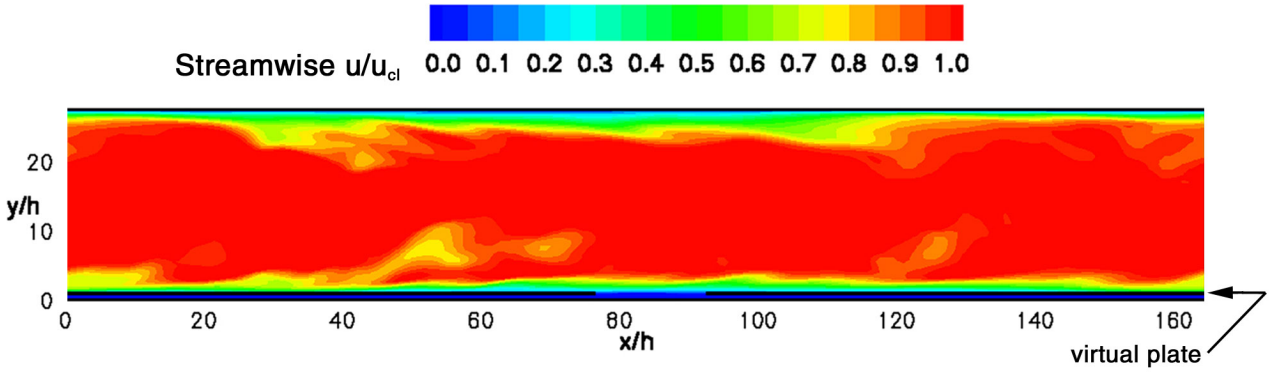

Figure 2: Contours of normalized streamwise (x) velocity on xy-plane through one slot (no actuation)

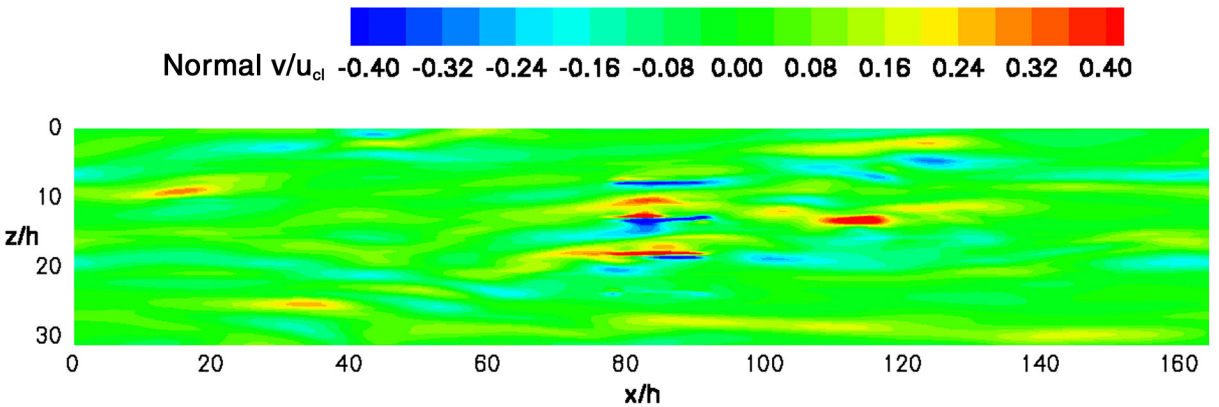

Figure 3: Contours of normalized normal velocity 4 wall units above the plate (no actuation)

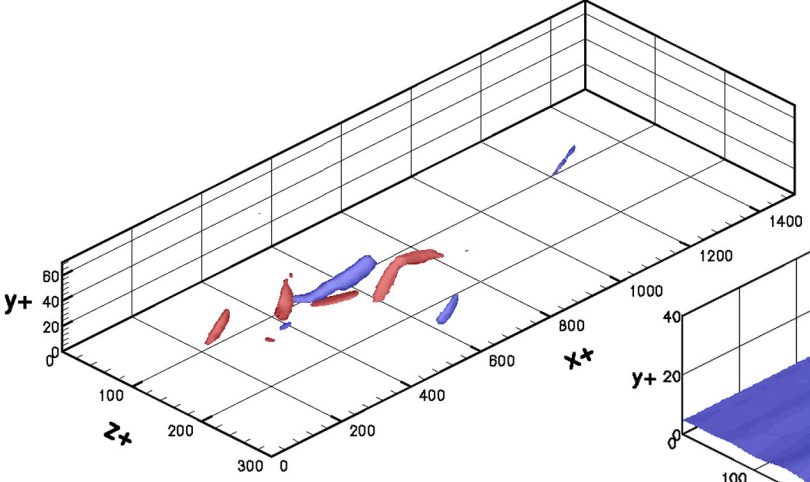

Figure 4: Contours of normalized Ω_x vorticity for no actuation case ($\Omega_x h/u_{cl} = \pm 0.8$)

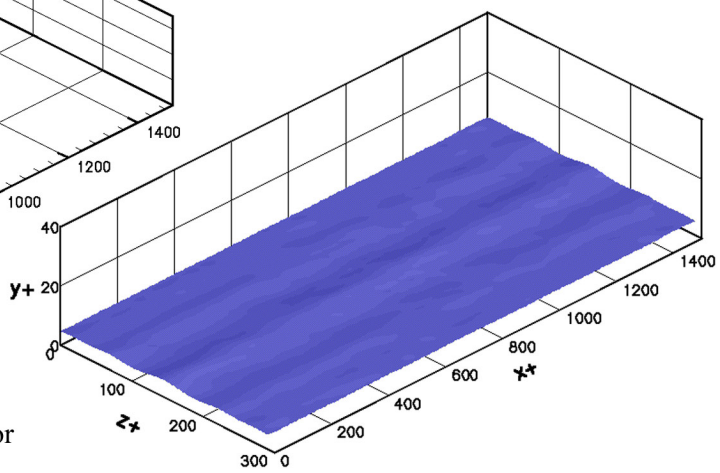

Figure 5: Time averaged iso-surface of streamwise velocty ($u^+ = 4$) for no actuation case.

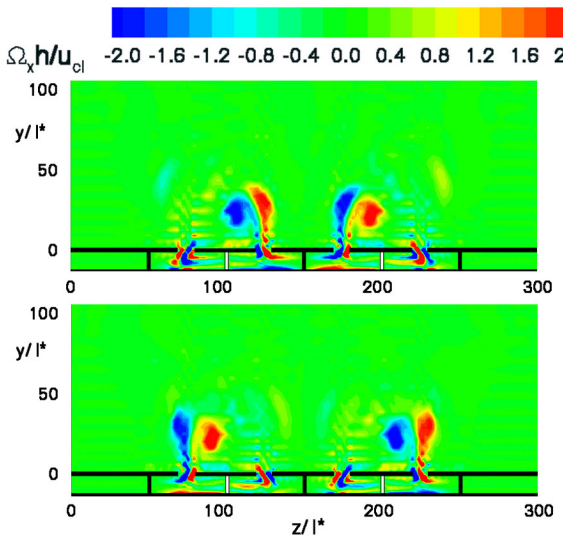

Figure 6: Contours of normalized Ω_x vorticity on zy-plane through actuators for no mean channel flow (top = "-++-" actuation, bottom = "+--+" actuation)

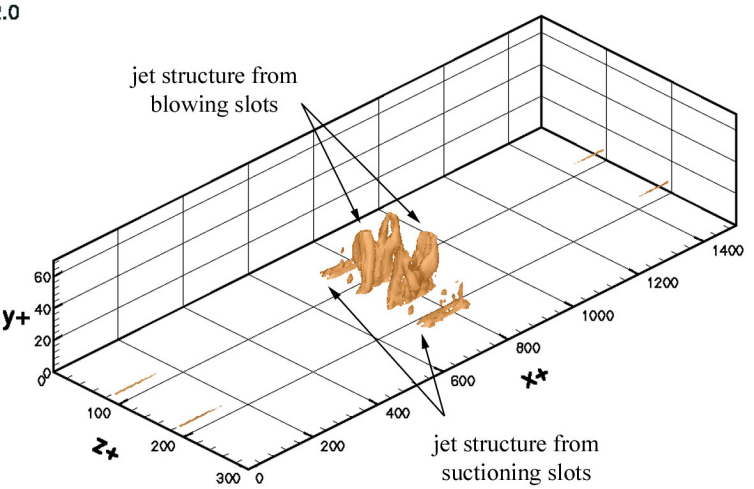

Figure 7(a): Contours of normalized instantaneous enstrophy for "-++-" actuation at T/2 ($|\underline{\Omega}|h/u_{cl} = 2$)

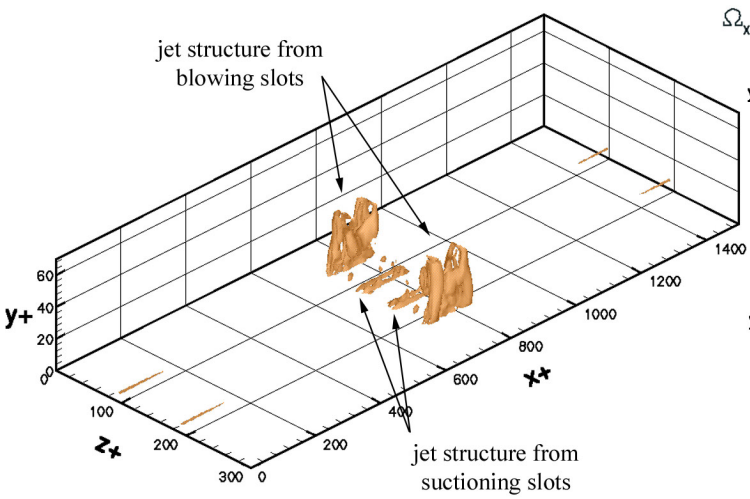

Figure 7(a): Contours of normalized instantaneous enstrophy for "+--+" actuation at T/2 ($|\underline{\Omega}|h/u_{cl} = 2$)

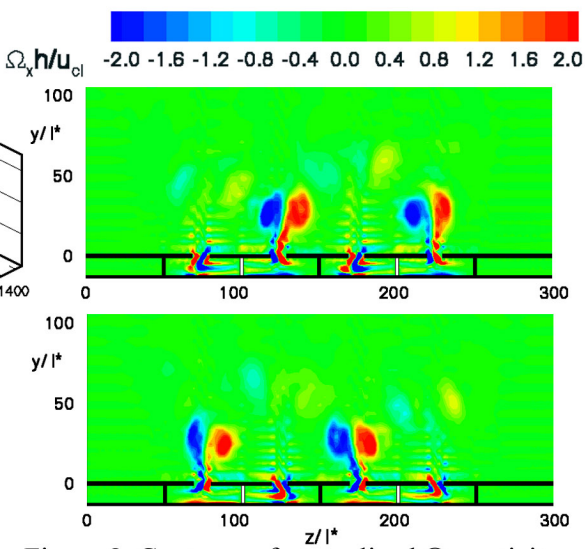

Figure 8: Contours of normalized Ω_x vorticity on zy-plane through actuators for no mean channel flow (top = "-+-+" actuation, bottom = "+-+-" actuation)

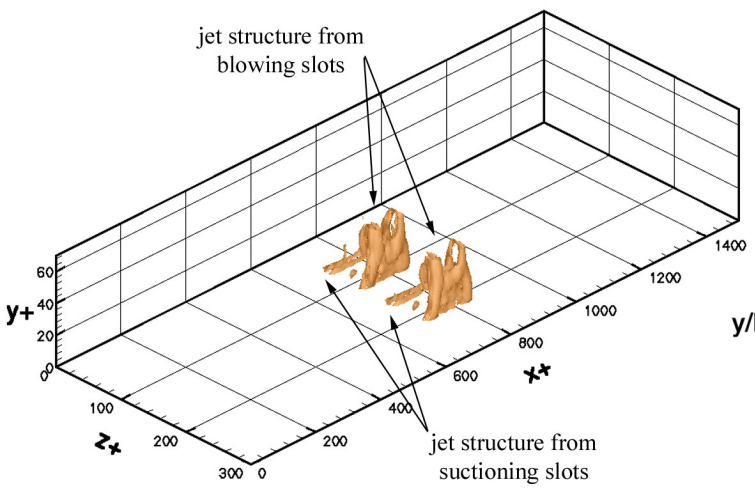

Figure 9: Contours of normalized instantaneous enstrophy for "-+-+" actuation at T/2 ($|\underline{\Omega}|h/u_{cl} = 2$)

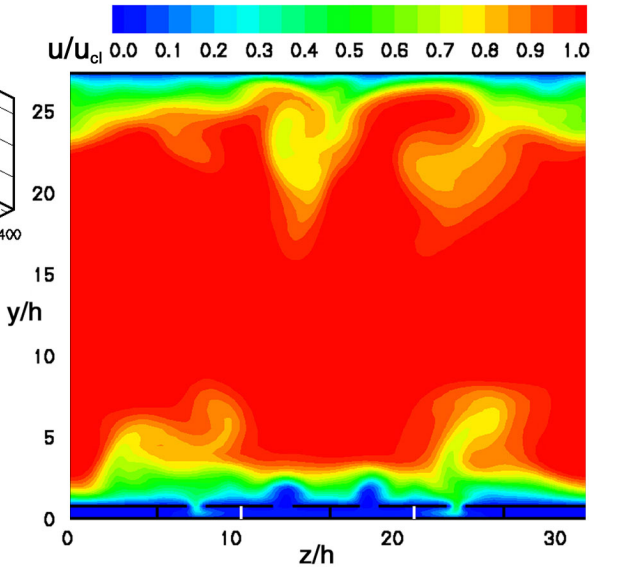

Figure 10: Contours of normalized streamwise vel. on zy-plane through actuators for quasi-steady "-++-" actuation

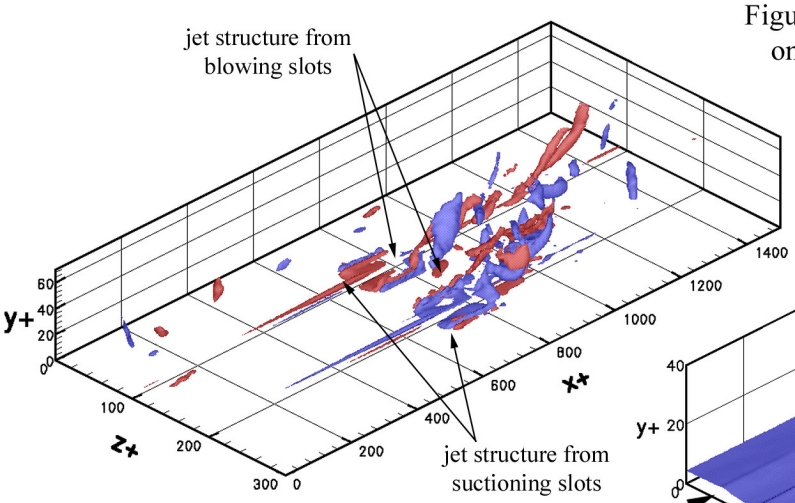

Figure 11: Contours of normalized Ω_x vorticity for quasi-steady "-++-" actuation ($\Omega_x h/u_{cl} = \pm 0.8$)

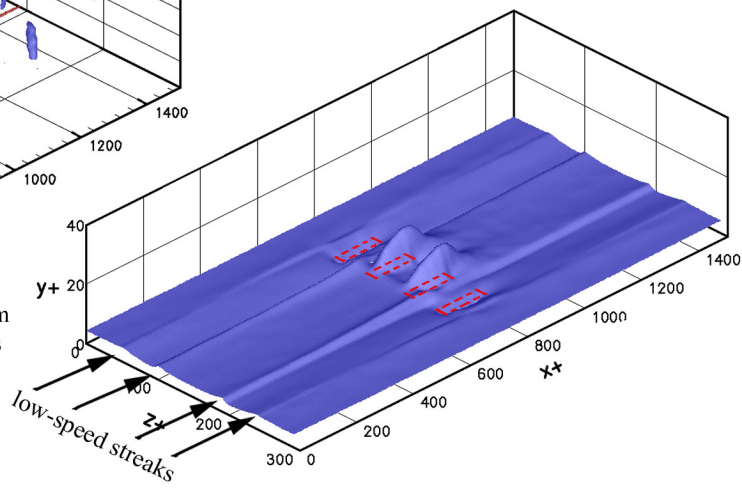

Figure 12: Time averaged iso-surface of streamwise vel. ($u^+ = 4$) for quasi-steady "-++-" actuation

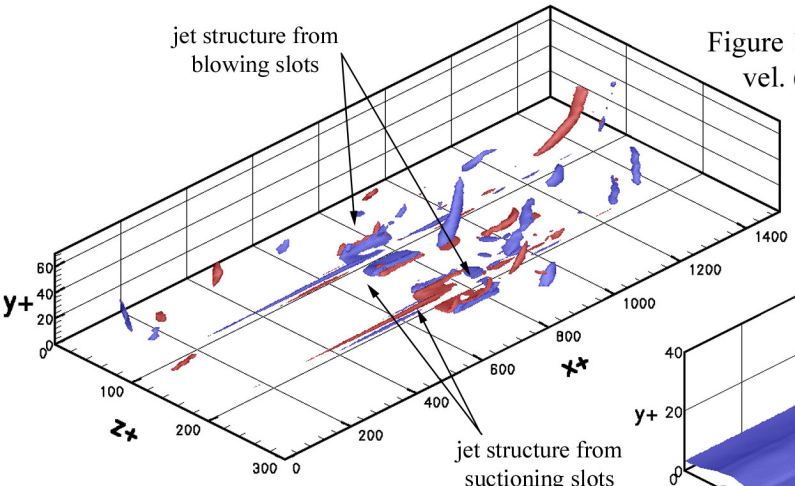

Figure 13: Contours of normalized Ω_x vorticity for quasi-steady "+--+" actuation ($\Omega_x h/u_{cl} = \pm 0.8$)

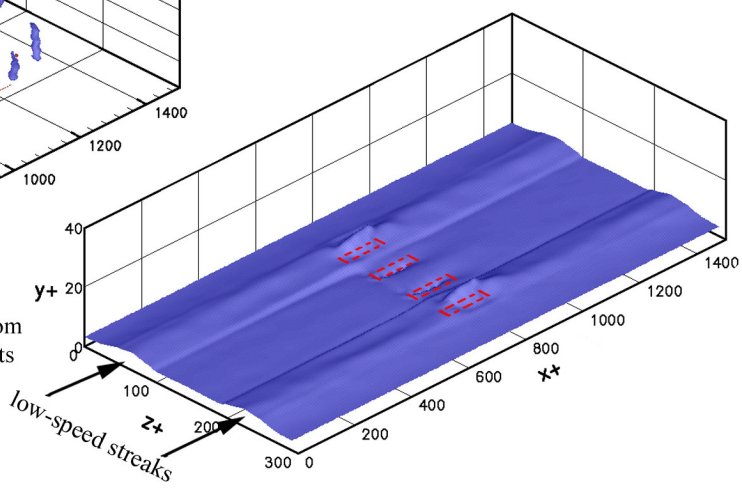

Figure 14: Time averaged iso-surface of streamwise vel. ($u^+ = 4$) for quasi-steady "+--+" actuation

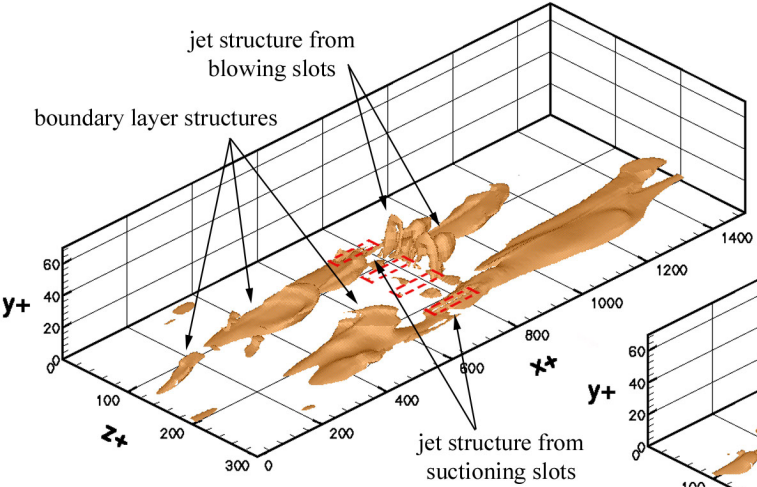

Figure 15: Contours of normalized instantaneous enstrophy for continuosly pulsed"-++-" mode at t = T ($|\underline{\Omega}|h/u_{cl} = 2$)

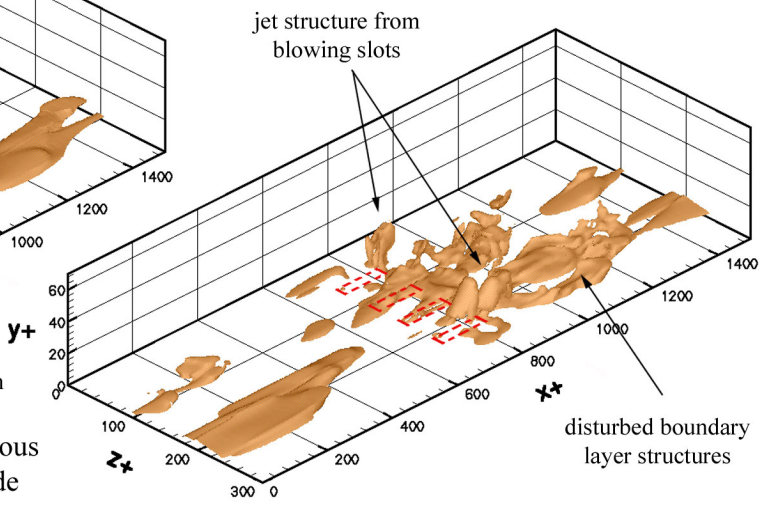

Figure 16: Contours of normalized instantaneous enstrophy for continuosly pulsed"-++-" mode at t = 4T ($|\underline{\Omega}|h/u_{cl} = 2$)

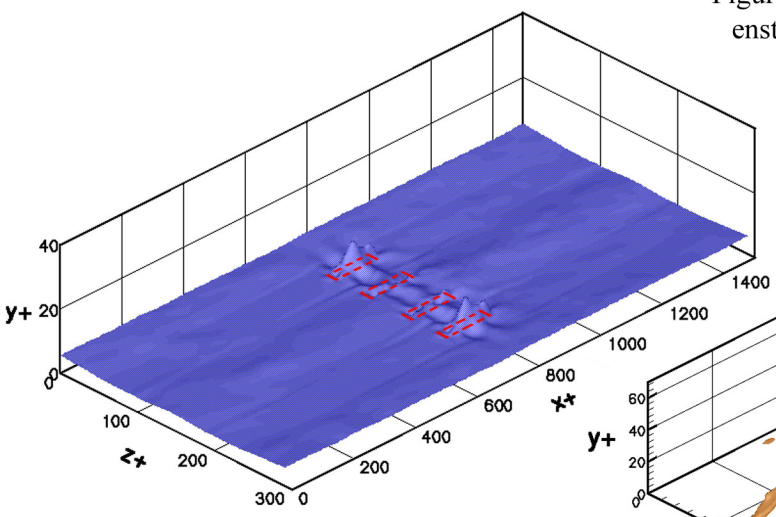

Figure 17: Time averaged iso-surface of streamwise vel. ($u^+ = 4$) for continously pulsed "-++-" mode

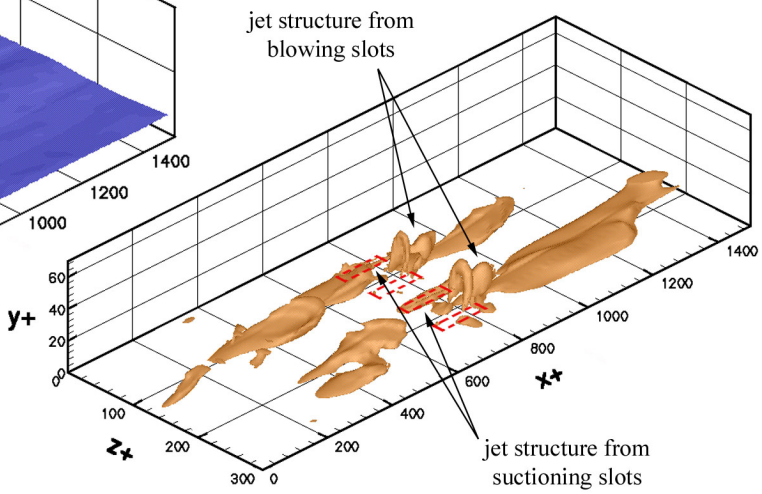

Figure 18: Contours of normalized instantaneous enstrophy for continuosly pulsed"-+-+" mode at t = T ($|\underline{\Omega}|h/u_{cl} = 2$)

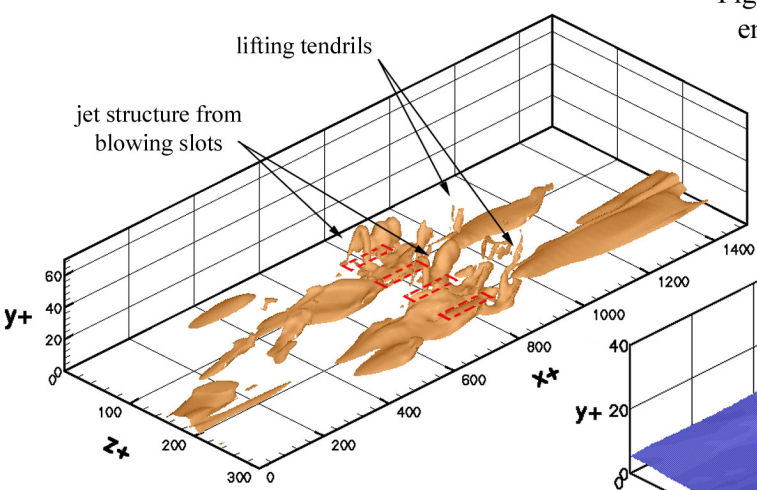

Figure 19: Contours of normalized instantaneous enstrophy for continuosly pulsed"-+-+" mode at t = 3T ($|\underline{\Omega}|h/u_{cl} = 2$)

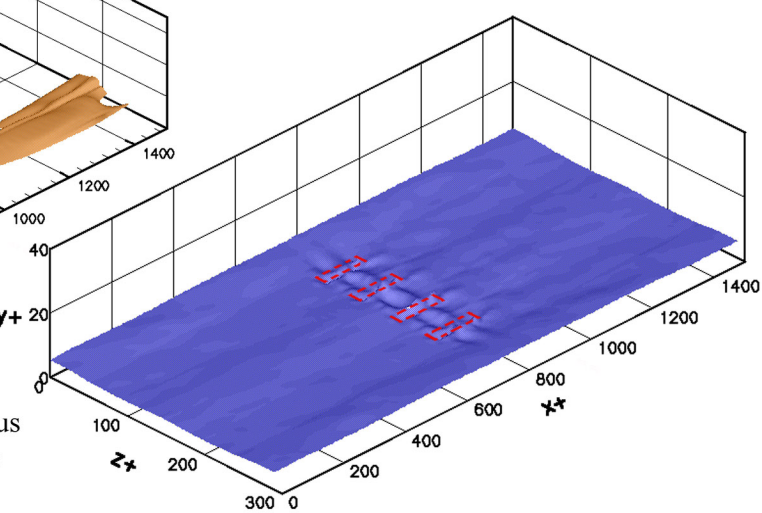

Figure 20: Time averaged iso-surface of streamwise vel. ($u^+ = 4$) for continously pulsed "-+-+" mode